DTU Library

Polarization-Dependent All-Dielectric Metasurface for Single-Shot Quantitative Phase Imaging

Engay, Einstom; Huo, Dewang; Malureanu, Radu; Bunea, Ada-Ioana; Lavrinenko, Andrei

[Link back to DTU Orbit](#)

Polarization-Dependent All-Dielectric Metasurface for Single-Shot Quantitative Phase Imaging

Einstom Engay,* Dewang Huo, Radu Malureanu, Ada-Ioana Bunea, and Andrei Lavrinenko

Cite This: https://doi.org/10.1021/acs.nanolett.1c00190

Read Online

ACCESS | 📊 Metrics & More | 📖 Article Recommendations | 🆂🅸 Supporting Information

ABSTRACT: Phase retrieval is a noninterferometric quantitative phase imaging technique that has become an essential tool in optical metrology and label-free microscopy. Phase retrieval techniques require multiple intensity measurements traditionally recorded by camera or sample translation, which limits their applicability mostly to static objects. In this work, we propose the use of a single polarization-dependent all-dielectric metasurface to facilitate the simultaneous recording of two images, which are utilized in phase calculation based on the transport-of-intensity equation. The metasurface acts as a multifunctional device that splits two orthogonal polarization components and adds a propagation phase shift onto one of them. As a proof-of-principle, we demonstrate the technique in the wavefront sensing of technical samples using a standard imaging setup. Our metasurface-based approach fosters a fast and compact configuration that can be integrated into commercial imaging systems.

Metasurface-based phase imaging setup

Recovered phase profile

KEYWORDS: all-dielectric metasurface, quantitative phase imaging, wavefront sensing, transport-of-intensity
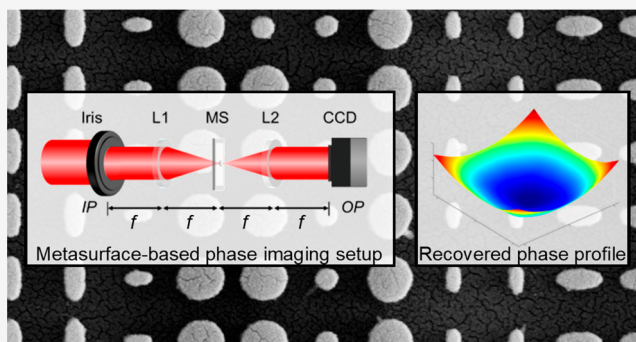
Metasurfaces are artificially engineered planar structures that have recently drawn significant attention due to their capability of modulating the properties of an incident optical wave, including its amplitude, wavefront, dispersion, and polarization properties.[1] For conventional optics, arbitrary wavefront control is realized with optical elements (e.g., lenses and prisms), phase plates, or spatial light modulators that all rely on gradual phase accumulation effects occurring as the wave propagates through an element. Instead, metasurfaces are composed of subwavelength units, called meta-atoms, whose optical and geometrical properties can be properly tuned to introduce abrupt phase changes into the incident light. All-dielectric metasurfaces have gained interest from the research community due to their low intrinsic losses, leading to a device efficiency higher than that of their plasmonic counterparts.[2] The desired phase delay in such metasurfaces can be achieved using high-index dielectric meta-atoms as waveguides.[3,4] The mismatch between the refractive indices of the meta-atom and the surrounding medium induces Fabry−Perot effects, resulting in the local modification of the phase of the incoming wave. By engineering the waveguide properties, for example, by appropriate combination of the meta-atoms' shape, size, and orientation, a $0-2\pi$ phase modulation can be realized. Owing to the subwavelength size and arrangement of the meta-atoms, metasurfaces circumvent the need for bulky components to achieve complex optical functionalities, which makes them conducive for compact integrated setups.[5,6] As such, metasurfaces have found applications for beam focusing,[7,8]

deflection,[9,10] holography,[11] and optical vortex generation.[12,13] Interestingly, these functionalities can be introduced independently and simultaneously in different polarization components of the incident light using a single metasurface.[14,15] Further advancement has recently been reported in the arbitrary polarization control along the beam propagation direction with a metasurface.[16] Tailored metasurfaces have also been shown to improve the imaging performance and facilitate super-resolution imaging and different contrast-enhancing modes in microscopy.[17−22]

Quantitative phase imaging (QPI) has emerged as an indispensable tool in label-free microscopy[23,24] and optical metrology.[25,26] QPI comprises a group of techniques that aims to quantitatively recover the phase of a complex field from available intensity measurements. In microscopy, weakly absorbing biological samples have marginal influence on the amplitude of the incident light, which makes them difficult to visualize under normal bright-field microscopes without adding contrast agents. Such samples, however, introduce substantial shift to the phase of the incident field. By detecting phase

modulations, QPI avoids the rigor of sample preparation and its possible side effects and allows access to morphologically relevant parameters such as the shape, size, thickness, and refractive index of the sample's structural components. In optical metrology, QPI facilitates wavefront sensing that has found applications in wavefront aberration correction and in optical inspection of technical samples,[27,28] including recent applications in characterizing metasurfaces.[29,30] QPI techniques are generally grouped into interferometric and non-interferometry-based methods, commonly referred to as phase retrieval methods. Interferometry-based techniques, such as digital holographic microscopy[31] and phase-shifting differential interference contrast (DIC) microscopy,[22,32] remain the benchmark of phase measurement schemes relying on the superposition of the scattered object field with a reference wave. From the recorded interference pattern, the object's complex field profile is reconstructed by digital postprocessing. While these techniques are more commonly used, two-beam interference strategies necessitate a high coherence degree of the source, minimal aberrations from the optical components, and high mechanical stability in the setup. Alternatively, phase retrieval methods, such as transport-of-intensity equation (TIE)-based methods, are less restrictive in terms of experimental requirements as they enable phase reconstruction from recorded images of the diffracted field without the need for a reference beam.[33−36] Phase retrieval utilizes the change in the intensity measurements as constraints in a mathematical inverse problem. In particular, TIE describes the relationship between the phase and the intensity gradient along the propagation direction.[35,37] In realization, two images, one focused and one defocused, are traditionally recorded by mechanical translation of the camera or the sample. From the focused intensity distribution and the axial intensity derivative estimated by a finite difference method, the phase information is calculated. The TIE-based phase retrieval has become attractive for QPI due to its simplicity, allowing for its straightforward integration with commercial microscopes.[38] A metasurface-based phase diffuser was recently demonstrated to facilitate phase retrieval using multiple axially displaced intensity measurements of the diffracted field.[17] However, individual recording of multiple images limited QPI to static objects. Meanwhile, two cascaded metasurfaces were employed to facilitate the single recording of intensities needed for phase calculation based on the phase-shifting DIC technique.[22]

In this work, we present an all-dielectric metasurface that facilitates quantitative phase imaging via TIE-based phase retrieval (MS-TIE) from *a single image recording step*. The traditional setup for TIE requires mechanically displacing either the camera or the sample to record the different intensity measurements needed for phase calculation, which limits phase reconstruction to static objects. To bypass this, we exploit the ability of all-dielectric metasurfaces to independently control two orthogonal polarization states and enable simultaneous capture of two images, eliminating the need for sample or camera displacement. Such a configuration results in a more stable setup, a faster acquisition system, and a potentially compact quantitative phase imaging configuration. Whereas our approach targets at the end a similar application to previous works on QPI,[17,22] the system presented herein comprises a single multifunctional metasurface and is fundamentally different, being noninterferometric and single-shot.

Figure 1a shows a schematic diagram of our proposed single-shot QPI setup. Image formation in the metasurface-based QPI
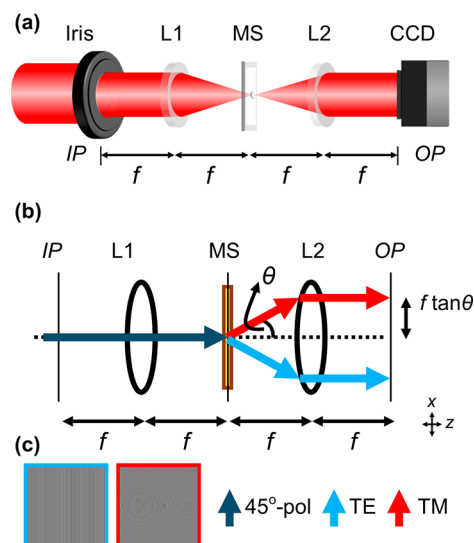

Figure 1. Quantitative phase imaging setup. (a) Schematic diagram of the metasurface (MS)-based quantitative phase imaging setup (MS-TIE). L1 and L2 form a 4*f* optical setup. The object is located at the input plane (IP), which can also coincide with the output (intermediate image plane) of a conventional microscope. The illumination is 45°-plane-polarized. The metasurface is placed at the Fourier plane and acts as a polarization-dependent optical filter that splits two orthogonal polarization components into two different directions and axially shifts one polarization from the other. (b) Introducing an angular displacement θ at the Fourier plane corresponds to a transverse shift $f \tan \theta$ at the output of the 4*f* setup. (c) Phase profiles of the metasurface to achieve polarization splitting and axial translation.

is described using Fourier transforms.[39] A 45°-plane-polarized beam is incident on the object. Lens L1 decomposes the complex input field $U_{in}(x,y) = A(x,y)\exp(i\varphi(x,y))$ into its Fourier components. The all-dielectric metasurface then acts as a polarization-dependent linear filter that imposes the following phase shifts to the transverse electric (TE) and transverse magnetic (TM) components of the impinging beam at the Fourier plane, independently:

$$\phi_{TE}(\eta, \nu) = \frac{2\pi}{\lambda}\eta \tan \theta \tag{1}$$

$$\phi_{TM}(\eta, \nu) = \frac{2\pi}{\lambda}\left(-\eta \tan \theta + \Delta z \sqrt{1 - \frac{1}{f^2}(\eta^2 + \nu^2)}\right) \tag{2}$$

where λ is the working wavelength, f is the focal length of the lenses, and η and ν are the spatial coordinates associated with the x and y directions at the Fourier plane. As described by eq 1, the metasurface phase profile is that of a blazed grating which angularly deflects the TE-polarized component by angle θ along the horizontal with respect to the optical axis. Similarly, the first term in eq 2 describes angular deflection of the TM component in the opposite direction. The metasurface essentially splits the orthogonal polarization components into two beams with an angular offset of 2θ and different optical paths. Furthermore, the second term in eq 2 corresponds to the phase term of the Rayleigh−Sommerfeld free-space
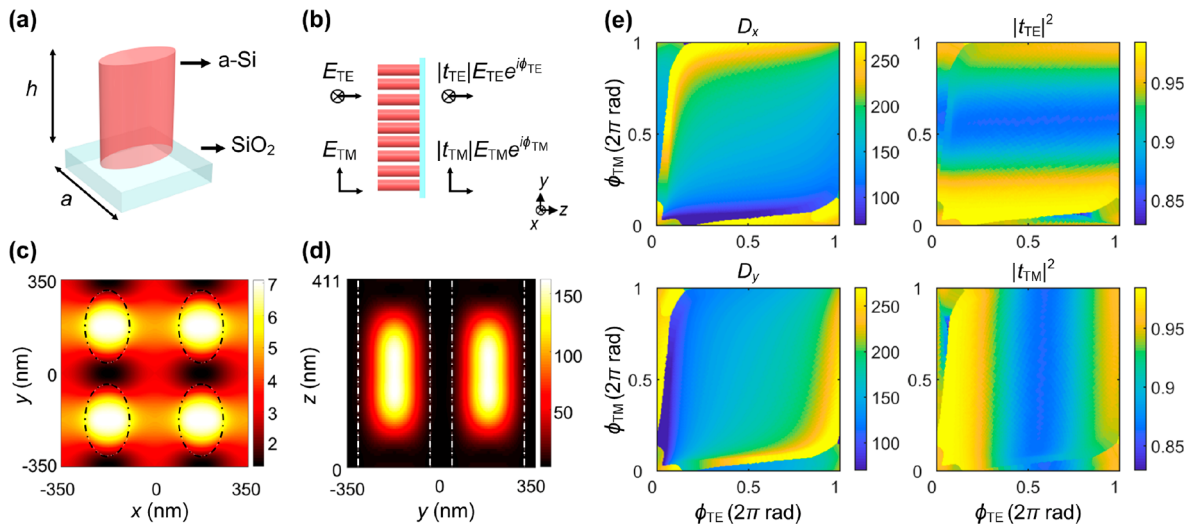
Figure 2. Metasurface design. (a) Unit cell of the metasurface consisting of amorphous silicon nanopillars on a fused silica substrate. The meta-atoms (h = 411 nm) that comprise the metasurface are periodically arranged in a square lattice with lattice constant, a = 350 nm. (b) Schematic for the numerical calculation of the transmission coefficients ($|t_{TE}|$, $|t_{TM}|$) and phase shifts ($|\phi_{TE}|$, $|\phi_{TM}|$) of the transmitted light after passing through the metasurface consisting of uniform pillars. (c,d) Magnetic energy density for D_x = 168 nm and D_y = 270 nm as seen from the (c) top view and (d) side view. The dashed lines in (c) and (d) represent the boundaries of the nanopillars. (e) Phase shift to elliptical diameter and transmittance maps.

propagation transfer function.[39] This simulates the axial translation of the TM component by an amount of Δz (defocus distance) relative to the TE-polarized wave. Figure 1b,c illustrates such multiple actions of the metasurface and the phase distributions to achieve them, respectively. See also section S1 of the Supporting Information (SI). After being passed through lens L2, the angular offset between the TE- and TM-polarized beams is converted into a lateral separation of $d = 2f \tan \theta$. The two beams are then simultaneously recorded by a camera. Mathematically, the complex output field at the camera plane is described by[39]

$$U_{out, TE(TM)}(x, y) = \mathfrak{F}^{-1}\{\mathfrak{F}\{U_{in}(x, y)\} \\ \times G(\eta, \nu)\exp(i\phi_{TE(TM)}(\eta, \nu))\} \quad (3)$$

where $\mathfrak{F}$ is the Fourier transform operator, $\mathfrak{F}^{-1}$ is its inverse, and (x,y) are the spatial coordinates at the input and output planes. After explicit evaluation of eq 3, the intensity pattern recorded by the camera is $I(x,y) = I_{TE}(x,y) + I_{TM}(x,y)$, where

$$I_{TE}(x, y) = |U_{in}(x + f \tan \theta, y) \otimes g(x, y)|^2 \quad (4)$$

$$I_{TM}(x, y) = \left| U_{in}(x - f \tan \theta, y) \right. \\ \left. \otimes \mathfrak{F}\left\{\exp\left(ik\Delta z\sqrt{1 - \frac{1}{f^2}(\eta^2 + \nu^2)}\right)\right\} \otimes g(x, y) \right|^2 \quad (5)$$

where $\otimes$ is the convolution operator. By adjusting the aperture at the input plane, the size of the two beams can be controlled to ensure that they fit within the sensor area and do not overlap. $g(x,y)$ is the Fourier transform of $G(\eta,\nu)$, which is a function that describes the finite width of the metasurface and can be approximated by a delta function for large enough metasurfaces. From the single image captured by the camera, numerical postprocessing is implemented to isolate and center the two intensity patterns described by eqs 4 and 5. For large

metasurfaces, this effectively reduces to the two intensity profiles obtained as if the camera was instead translated:

$$I_1(x, y) = |U_{in}(x, y)|^2 \quad (6)$$

$$I_2(x, y) = \left| U_{in}(x, y) \otimes \mathfrak{F}\left\{\exp\left(ik\Delta z\sqrt{1 - \frac{1}{f^2}(\eta^2 + \nu^2)}\right)\right\}\right|^2 \quad (7)$$

The TIE arises from the parabolic wave equation and relates $\varphi(x,y)$ of the input field to its axial intensity derivative by[33]

$$-k\frac{\partial I(x, y)}{\partial z} = \nabla_\perp \cdot [I(x, y)\nabla_\perp \varphi(x, y)] \quad (8)$$

where k is the wavenumber $2\pi/\lambda$, $\nabla_\perp$ is the two-dimensional gradient operator over the transverse coordinates (x,y), and z is the coordinate along the optical axis. Here, $I(x,y)$ is the focused intensity I_1, and the axial intensity derivative is estimated by $\frac{dI}{dz} = \frac{I_2 - I_1}{\Delta z}$. Different numerical approaches can be implemented to evaluate eq 8, and each entails satisfying specific boundary conditions and certain requirements in the recorded intensities that can be rather difficult to achieve in experiments.[35] Recently, an iterative algorithm has been reported to relax such requirements and provide a universal solution to TIE.[37] This iterative algorithm was implemented here and is further detailed in the SI section S2.

Figure 2a shows the unit cell of the metasurface consisting of an amorphous silicon nanopillar on a fused silica substrate. To calculate the transmission coefficients ($|t_{TE}|$ and $|t_{TM}|$) and phase shifts (ϕ_{TE} and ϕ_{TM}) imparted to the incident wave, full-wave simulations with the finite-difference time-domain (FDTD) method were implemented, as schematically shown in Figure 2b for elliptical nanopillars periodically arranged in a square lattice. The height of the nanopillars is h = 411 nm, the lattice constant is a = 350 nm, and the wavelength is λ = 850 nm. The calculations were done for different combinations of the lateral parameters D_x and D_y for TE- and TM-polarized

incident waves. As shown in Figure 2c,d, the magnetic field energy density is concentrated within the nanopillars, and weak coupling is observed between neighboring meta-atoms. Thus, each meta-atom can be regarded as a pixel element in the metasurface design which locally modifies the wavefront. From the FDTD calculations, the phase-to-diameter conversion maps shown in Figure 2e were obtained, as detailed in the SI section S3. The corresponding maps of the transmission coefficients illustrate high transmission, >70%, for all nanopillars used in the design. From the analytic expressions of the phase profiles in eqs 1 and 2, the metasurface profile was generated using 2000 × 2000 nanopillars with Δz = 5 mm and subsequently fabricated using a standard electron beam lithography technique and Bosch etch process,[40] as detailed in sections S3 and S4 of the SI. Figure 3 shows top-view (a,b)
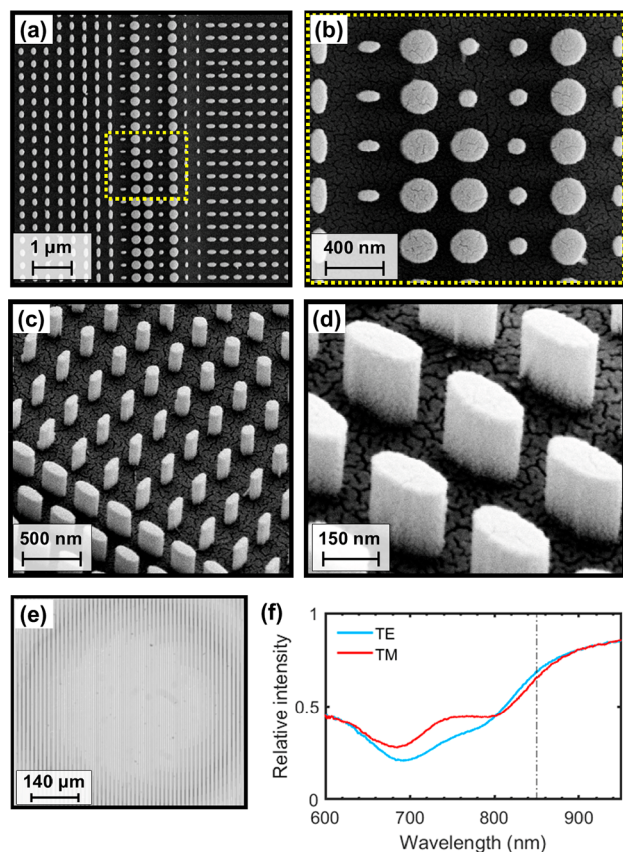

Figure 3. Metasurface characterization. (a,b) Top-view and (c,d) tilted-view 30° scanning electron micrographs and (e) bright-field image of the metasurface. (f) Measured transmission spectra of the metasurface for TE- and TM-polarized incident beams.

and tilted-view (c,d) scanning electron microscopy images, and a bright-field image (e) of the fabricated metasurface. Figure 3f shows the measured transmission spectra of the metasurface, with overall transmission efficiencies of 68 and 65% for the TE- and TM-polarized beams, respectively, for λ = 850 nm. These values are slightly lower than expected from the FDTD calculations, yet comparable with those reported in the literature using similar systems.[41] From Fourier space measurements, it was verified that the angular deflections are as designed: $\theta_{TE/TM,des}$ = 0.070 rad, $\theta_{TE/TM,meas}$ = 0.071 rad corresponding to lateral beam displacements of $d_{TE/TM}$ = ∓3.5 mm from the camera center.

As a proof-of-concept, we validated the use of the metasurface-based TIE (MS-TIE) in wavefront sensing. We used a convex lens (focal length: 250 mm) placed behind a square aperture (width: 1.6 mm) as a technical sample. See Figure S6 of the SI for the full setup. The focal length of the lenses used in the 4f system is 50 mm. Figure 4a shows the image obtained from the camera without the metasurface. Figure 4b,c shows the cropped images corresponding to the TE-polarized (focused image) and TM-polarized (defocused image, Δz = 5 mm) beams, respectively, with the metasurface aligned in the setup. In principle, Figure 4b should be a focused image of the aperture. However, the metasurface also acts effectively as a low-pass filter that truncates the high-frequency components of the object, resulting in the blurred image shown in Figure 4b. In principle, this issue can be addressed by simply increasing the size of the metasurface. In our Fourier optics simulations (detailed in SI section S5), the size of the metasurface was deemed enough to provide a good phase reconstruction (Figure 4e) for this technical sample, comparing it with the analytic phase profile shown in Figure 4d. Figure 4f shows the experimentally reconstructed phase profile using our MS-TIE technique. The reconstruction was compared to that of the conventional TIE (C-TIE), shown in Figure 4g, which was implemented using the same setup but with the two images recorded by displacing the camera by 1.5 mm. In principle, estimation of the intensity gradient can be obtained more accurately with smaller Δz, but due to design and fabrication limitations, the introduced defocus distance by the metasurface is slightly larger than the one used for C-TIE. Both TIE reconstructions were further benchmarked against the reconstruction (Figure 4h) with the multiple-plane phase retrieval (MPR) technique (see SI section S7).[36] Qualitatively, the retrieved phase profile from MS-TIE closely resembles that of the analytic wavefront and those from C-TIE and MPR, apart from the observed artifacts that can be attributed to imperfections in the metasurface. The line profiles of the unwrapped reconstructed phase from MS-TIE and C-TIE approximate each other, as shown in Figure 4i. The root-mean-square errors $\left(\text{RMSE} = \sqrt{\frac{1}{N} \sum_{i=1}^{N} \left(\varphi_{ex} - \varphi_{an} \right)^2} \right)$ between the experimentally retrieved and the analytic wrapped phase distributions were calculated, where $\text{RMSE}_{MS\text{-}TIE}$ = 0.6632, $\text{RMSE}_{C\text{-}TIE}$ = 0.7804, and RMSE_{MPR} = 0.7772. The semblance of the MS-TIE reconstruction with the other results shows the potential of the proposed MS-TIE technique as an effective alternative to existing methods for QPI. The quantitative phase measurement also allows the transformation to the optical thickness profile of the sample, as shown in Figure 4j.

We further used the setup to reconstruct the phase profile of a concave lens (f = −100 mm). Figure 5a−c shows similar phase distributions retrieved using MS-TIE and C-TIE, which further serves as proof that MS-TIE can be as effective as C-TIE. Figure 5d shows the continuous phase profile from the TIE calculation. Finally, the same metasurface was used to phase-image three phase-only vertical bars from the USAF resolution target viewed under a normal bright-field microscope, whose conjugate image plane coincided with the square aperture of the MS-TIE, as further detailed in the SI. Figure 5e,f shows the phase images from MS-TIE and C-TIE, respectively. Here, the MS-TIE was able to discriminate the phase steps from the background but admittedly not as well as the C-TIE. The central line profile in Figure 5g and the continuous phase map in Figure 5h reveal that, for MS-TIE,
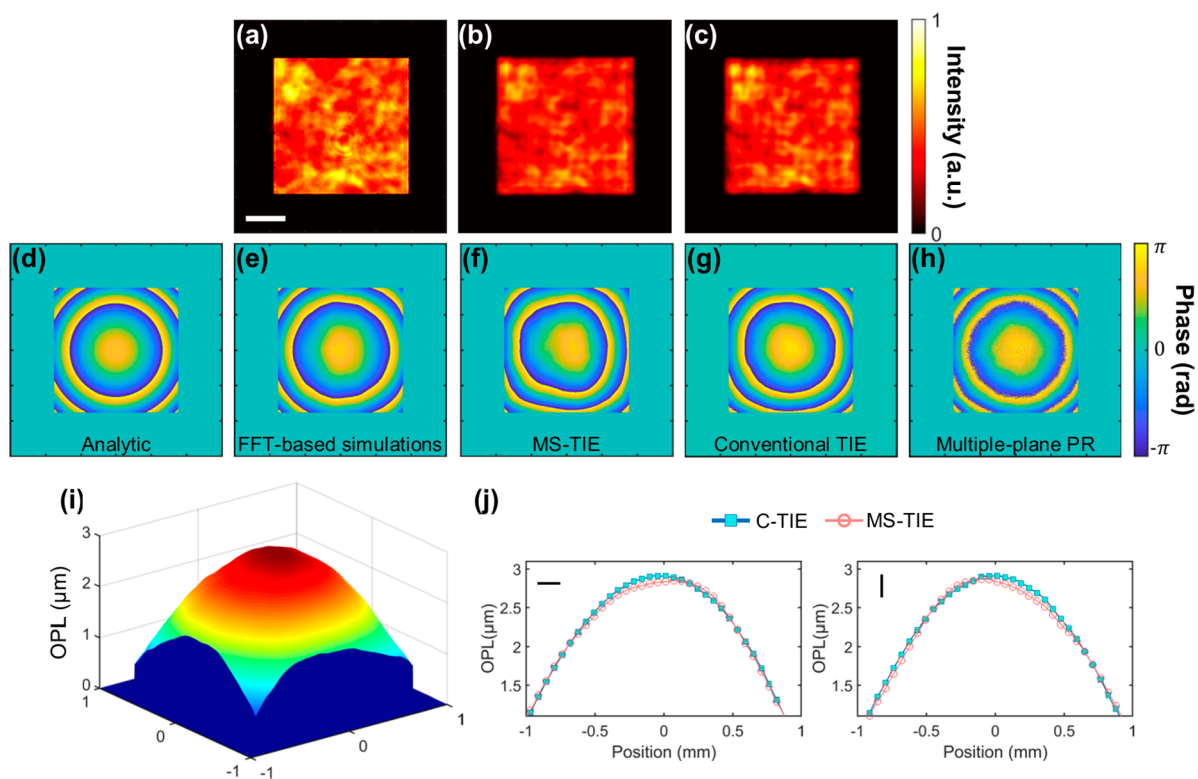
Figure 4. Wavefront sensing using MS-based TIE. (a) Bright-field image (false color) of the technical sample consisting of a lens placed behind a square aperture. Scale bar: 0.5 mm. (b,c) Cropped images from the split TE and TM beams, respectively, using the MS-based TIE. (d) Analytic phase profile of a lens with f = 250 mm. (e−h) Wrapped reconstructed phase profiles using (e) fast Fourier transform (FFT)-based simulations of MS-TIE, (f) experimental MS-TIE, (g) conventional TIE with camera displacement d = 5 mm, and (h) multiple-plane phase retrieval using 25 intensity measurements. (i) Optical thickness profile obtained from the reconstructed phase distribution. (j) Line profiles of the phase reconstructions from MS-TIE (blue plot) and C-TIE (red plot). Solid lines indicate the direction of the scan.
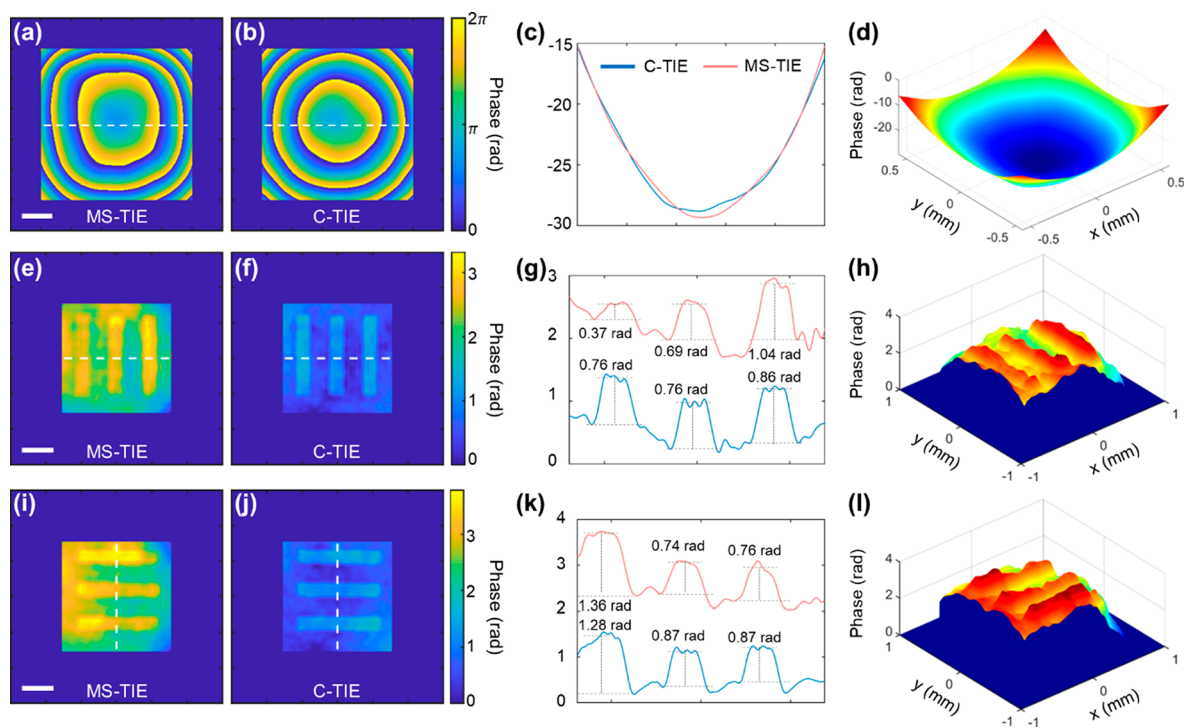
Figure 5. MS-based TIE for phase imaging. Wrapped phase profile of a concave lens (f = 150 mm) reconstructed using (a) MS-TIE and (b) C-TIE. Scale bar: 200 μm. (c) Line profile at the center of the phase reconstructions. Reconstructed phase profiles of (e−h) vertical and (i−l) horizontal phase bars and their corresponding line profiles. Scale bar: 20 μm at the sample plane for the phase bars. (d,h,l) 3D map of the continuous phase distribution retrieved from MS-TIE.

the phase steps for the three bars vary largely, 0.37, 0.69, and 1.04 rad, in contrast to the C-TIE, 0.76, 0.76, and 0.86 rad. An x-dependent phase discrepancy is obvious from the reconstruction, which is more evident for large phase gradients like those introduced by the bars. From our fast Fourier transform (FFT)-based simulations, this is caused mainly by the finite sizes of the metasurface, further compounded by the deviation of the metasurface phase profile from the analytic as described in eqs 1 and 2. With our current metasurface, this can be mitigated by aligning more crucial features along the y direction, as shown in Figure 5i−l. Here, the reconstructed phase step values of the three horizontal bars have pronouncedly decreased variations for the MS-TIE, albeit still slightly deviating from the values obtained using C-TIE. While this means a need to further optimize the device design and fabrication to measure acute phase variations in small areas but within the limit of the TIE assumptions, we show for the first time a promising single polarization-dependent metasurface to facilitate QPI.

One obvious limitation of the current setup is the size of the metasurface ($700 \times 700\ \mu m^2$), as mentioned above, which dictates the lateral resolution that can be achieved. As modeled in eqs 4 and 5, this can be circumvented by increasing the size of the metasurface. More importantly, simulations show that the limited size is the main factor causing the observed phase artifacts in the reconstructed profiles for the phase bars. Additionally, as discussed previously,[35] large defocus distances also contribute to inaccurate phase reconstructions due to the inaccurate estimation of the axial intensity derivative. From our simulations, it was deemed that, as a first demonstration, the size and the defocus distance were enough to obtain accurate phase reconstructions for samples that have low phase gradients (i.e., lenses). Second, the simultaneous recording of two images comes at the expense of the system's effective field of view, which has become smaller than that in the case when the full camera sensor width is utilized to capture one image at a time. Although the field of view is sacrificed, the ability to simultaneously capture the intensities will allow for QPI of dynamic events, and it can be alleviated by using larger camera sensors. Lastly, an advantage of conventional setups is the tunability of the defocus distance, which is known to be object-dependent. Currently, distance tuning is not available in our metasurface device. Nonetheless, this does not preclude the use of fixed and optimized metasurfaces to work for diverse types of phase objects. In addition, the flourishing research on tunable metasurfaces indicates the viability of active displacement setting in the future.[42−44] An obvious next step is the application of MS-TIE to biological imaging. This would entail further optimization of the metasurface design (i.e., using other unit cell designs to better approximate the desired phase combinations) with a larger cross section to allow for better tuning of the defocus distance and to increase the frequency cutoff of the system.

In summary, we presented a single polarization-dependent all-dielectric metasurface as an enabling device for quantitative phase reconstruction. The metasurface allows the simultaneous recording of two images by splitting the TE and TM components of the incident wave and introducing an axial shift to the TM component. The two images were used as constraints to retrieve the phase information by iterative calculation of the transport-of-intensity equation. We implemented the proposed technique in wavefront sensing of technical samples. Compared to existing methods that aim for single-shot quantitative phase measurement, our proposed technique only requires a single metasurface that can be conveniently placed at a conjugate to the back focal plane of the objective in a microscope. This technique exhibits great potential to facilitate simple, compact, and rapid QPI, ideal for optical metrology and live label-free microscopy applications.

■ ASSOCIATED CONTENT

Ⓢ Supporting Information

The Supporting Information is available free of charge at https://pubs.acs.org/doi/10.1021/acs.nanolett.1c00190.

> Derivation of the metasurface phase profile; description of the transport-of-intensity equation; description of the FDTD calculations; metasurface fabrication process flow; Fourier optics-based simulations of the metasurface-based imaging system; optical characterization setup; description of the multiple-plane phase retrieval (PDF)

■ AUTHOR INFORMATION

Corresponding Author

Einstom Engay − *DTU Fotonik, Department of Photonics Engineering and DTU Nanolab, National Centre for Nano Fabrication and Characterization, Technical University of Denmark, Kgs. Lyngby 2800, Denmark;* ⓞ orcid.org/0000-0002-2415-0316; Email: einen@dtu.dk

Authors

Dewang Huo − *DTU Fotonik, Department of Photonics Engineering, Technical University of Denmark, Kgs. Lyngby 2800, Denmark; Institute of Modern Optics, Department of Physics, Harbin Institute of Technology, Harbin 15000, China*

Radu Malureanu − *DTU Fotonik, Department of Photonics Engineering, Technical University of Denmark, Kgs. Lyngby 2800, Denmark;* ⓞ orcid.org/0000-0002-6093-5030

Ada-Ioana Bunea − *DTU Nanolab, National Centre for Nano Fabrication and Characterization, Technical University of Denmark, Kgs. Lyngby 2800, Denmark*

Andrei Lavrinenko − *DTU Fotonik, Department of Photonics Engineering, Technical University of Denmark, Kgs. Lyngby 2800, Denmark;* ⓞ orcid.org/0000-0001-8853-2033

Complete contact information is available at:
https://pubs.acs.org/10.1021/acs.nanolett.1c00190

Notes

The authors declare no competing financial interest.

■ REFERENCES

(1) Genevet, P.; Capasso, F.; Aieta, F.; Khorasaninejad, M.; Devlin, R. Recent Advances in Planar Optics: From Plasmonic to Dielectric Metasurfaces. *Optica* **2017**, *4* (1), 139.

(2) Kamali, S. M.; Arbabi, E.; Arbabi, A.; Faraon, A. A Review of Dielectric Optical Metasurfaces for Wavefront Control. *Nanophotonics* **2018**, *7* (6), 1041−1068.

(3) Mahmood, N.; Kim, I.; Mehmood, M. Q.; Jeong, H.; Akbar, A.; Lee, D.; Saleem, M.; Zubair, M.; Anwar, M. S.; Tahir, F. A.; Rho, J. Polarisation Insensitive Multifunctional Metasurfaces Based on All-Dielectric Nanowaveguides. *Nanoscale* **2018**, *10* (38), 18323−18330.

(4) Arbabi, A.; Horie, Y.; Bagheri, M.; Faraon, A. Dielectric Metasurfaces for Complete Control of Phase and Polarization with Subwavelength Spatial Resolution and High Transmission. *Nat. Nanotechnol.* **2015**, *10* (11), 937−943.

(5) Wang, Z.; Li, T.; Soman, A.; Mao, D.; Kananen, T.; Gu, T. On-Chip Wavefront Shaping with Dielectric Metasurface. *Nat. Commun.* **2019**, *10* (1), 1−7.

(6) Brongersma, M. L. The Road to Atomically Thin Metasurface Optics. *Nanophotonics* **2020**, *10* (1), 643−654.

(7) Shalaginov, M. Y.; An, S.; Yang, F.; Su, P.; Lyzwa, D.; Agarwal, A. M.; Zhang, H.; Hu, J.; Gu, T. Single-Element Diffraction-Limited Fisheye Metalens. *Nano Lett.* **2020**, *20*, 7429−7437.

(8) Decker, M.; Chen, W. T.; Nobis, T.; Zhu, A. Y.; Khorasaninejad, M.; Bharwani, Z.; Capasso, F.; Petschulat, J. Imaging Performance of Polarization-Insensitive Metalenses. *ACS Photonics* **2019**, *6* (6), 1493−1499.

(9) Mohammadi Estakhri, N.; Alu, A. Wave-Front Transformation with Gradient Metasurfaces. *Phys. Rev. X* **2016**, *6* (4), 1−17.

(10) Ni, Y.; Chen, S.; Wang, Y.; Tan, Q.; Xiao, S.; Yang, Y. Metasurface for Structured Light Projection over 120° Field of View. *Nano Lett.* **2020**, *20* (9), 6719−6724.

(11) Gao, H.; Wang, Y.; Fan, X.; Jiao, B.; Li, T.; Shang, C.; Zeng, C.; Deng, L.; Xiong, W.; Xia, J.; Hong, M. Dynamic 3D Meta-Holography in Visible Range with Large Frame Number and High Frame Rate. *Sci. Adv.* **2020**, *6* (28), eaba8595.

(12) Vertchenko, L.; Shkondin, E.; Malureanu, R.; Monken, C. Laguerre-Gauss Beam Generation in IR and UV by Subwavelength Surface-Relief Gratings. *Opt. Express* **2017**, *25* (6), 5917−5926.

(13) Piccardo, M.; Ambrosio, A. Recent Twists in Twisted Light: A Perspective on Optical Vortices from Dielectric Metasurfaces. *Appl. Phys. Lett.* **2020**, *117* (14), 140501−1.

(14) Ding, F.; Chang, B.; Wei, Q.; Huang, L.; Guan, X.; Bozhevolnyi, S. I. Versatile Polarization Generation and Manipulation Using Dielectric Metasurfaces. *Laser Photonics Rev.* **2020**, *14*, 2000116.

(15) Hu, Y.; Wang, X.; Luo, X.; Ou, X.; Li, L.; Chen, Y.; Ping Yang; Wang, S.; Duan, H. All-Dielectric Metasurfaces for Polarization Manipulation: Principles and Emerging Applications. *Nanophotonics* **2020**, *9* (12), 3755−3780.

(16) Dorrah, A. H.; Rubin, N. A.; Zaidi, A.; Tamagnone, M.; Capasso, F. Metasurface Optics for On-Demand Polarization Transformations along the Optical Path. *Nat. Photonics* **2021**, *15*, 287−296.

(17) Kwon, H.; Arbabi, E.; Kamali, S. M.; Faraji-Dana, M.; Faraon, A. Computational Complex Optical Field Imaging Using a Designed Metasurface Diffuser. *Optica* **2018**, *5* (8), 924.

(18) Rubin, N. A.; D'Aversa, G.; Chevalier, P.; Shi, Z.; Chen, W. T.; Capasso, F. Matrix Fourier Optics Enables a Compact Full-Stokes Polarization Camera. *Science (Washington, DC, U. S.)* **2019**, *365* (6448), eaax1839.

(19) Holsteen, A. L.; Lin, D.; Kauvar, I.; Wetzstein, G.; Brongersma, M. L. A Light-Field Metasurface for High-Resolution Single-Particle Tracking. *Nano Lett.* **2019**, *19* (4), 2267−2271.

(20) Lee, D.; Gwak, J.; Badloe, T.; Palomba, S.; Rho, J. Metasurfaces-Based Imaging and Applications: From Miniaturized Optical Components to Functional Imaging Platforms. *Nanoscale Adv.* **2020**, *2* (2), 605−625.

(21) Huo, P.; Zhang, C.; Zhu, W.; Liu, M.; Zhang, S.; Zhang, S.; Chen, L.; Lezec, H. J.; Agrawal, A.; Lu, Y.; Xu, T. Photonic Spin-Multiplexing Metasurface for Switchable Spiral Phase Contrast Imaging. *Nano Lett.* **2020**, *20* (4), 2791−2798.

(22) Kwon, H.; Arbabi, E.; Kamali, S. M.; Faraji-Dana, M. S.; Faraon, A. Single-Shot Quantitative Phase Gradient Microscopy Using a System of Multifunctional Metasurfaces. *Nat. Photonics* **2020**, *14* (2), 109−114.

(23) Park, Y. K.; Depeursinge, C.; Popescu, G. Quantitative Phase Imaging in Biomedicine. *Nat. Photonics* **2018**, *12* (10), 578−589.

(24) Cacace, T.; Bianco, V.; Ferraro, P. Quantitative Phase Imaging Trends in Biomedical Applications. *Opt. Lasers Eng.* **2020**, *135*, 106188.

(25) Marrugo, A. G.; Gao, F.; Zhang, S. State-of-the-Art Active Optical Techniques for Three-Dimensional Surface Metrology: A Review [Invited]. *J. Opt. Soc. Am. A* **2020**, *37* (9), B60.

(26) De Groot, P. J. A Review of Selected Topics in Interferometric Optical Metrology. *Rep. Prog. Phys.* **2019**, *82*, 056101.

(27) Almoro, P. F.; Gundu, P. N.; Hanson, S. G. Phase Retrieval With Speckle Illumination. *Opt. Lett.* **2009**, *34* (4), 521−523.

(28) Niu, M.; Luo, G.; Shu, X.; Qu, F.; Zhou, S.; Ho, Y.-P.; Zhou, R.; Zhao, N. A Portable Quantitative Phase Microscope for Material Metrology and Biological Imaging. *Photonics Res.* **2020**, *8* (7), 1253−1259.

(29) Bouchal, P.; Dvořák, P.; Babocký, J.; Bouchal, Z.; Ligmajer, F.; Hrtoň, M.; Křápek, V.; Faßbender, A.; Linden, S.; Chmelík, R.; Sikola, T. High-Resolution Quantitative Phase Imaging of Plasmonic Metasurfaces with Sensitivity down to a Single Nanoantenna. *Nano Lett.* **2019**, *19*, 1242−1250.

(30) Babocký, J.; Křížová, A.; Štrbková, L.; Kejík, L.; Ligmajer, F.; Hrtoň, M.; Dvořák, P.; Týč, M.; Čolláková, J.; Křápek, V.; Kalousek, R.; Chmelík, R.; Šikola, T. Quantitative 3D Phase Imaging of Plasmonic Metasurfaces. *ACS Photonics* **2017**, *4* (6), 1389−1397.

(31) Kemper, B.; Von Bally, G. Digital Holographic Microscopy for Live Cell Applications and Technical Inspection. *Appl. Opt.* **2008**, *47* (4), A52−A61.

(32) Arnison, M. R.; Larkin, K. G.; Sheppard, C. J. R.; Smith, N. I.; Cogswell, C. J. Linear Phase Imaging Using Differential Interference Contrast Microscopy. *J. Microsc.* **2004**, *214* (1), 7−12.

(33) Teague, M. R. Deterministic Phase Retrieval: A Green'S Function Solution. *J. Opt. Soc. Am.* **1983**, *73* (11), 1434−1441.

(34) Zuo, C.; Chen, Q.; Qu, W.; Asundi, A. Noninterferometric Single-Shot Quantitative Phase Microscopy. *Opt. Lett.* **2013**, *38* (18), 3538.

(35) Zuo, C.; Li, J.; Sun, J.; Fan, Y.; Zhang, J.; Lu, L.; Zhang, R.; Wang, B.; Huang, L.; Chen, Q. Transport of Intensity Equation: A Tutorial. *Opt. Lasers Eng.* **2020**, *135*, 106187.

(36) Almoro, P.; Pedrini, G.; Osten, W. Complete Wavefront Reconstruction Using Sequential Intensity Measurements of a Volume Speckle Field. *Appl. Opt.* **2006**, *45* (34), 8596−8605.

(37) Zhang, J.; Chen, Q.; Sun, J.; Tian, L.; Zuo, C. On a Universal Solution to the Transport-of-Intensity Equation. *Opt. Lett.* **2020**, *45* (13), 3649−3652.

(38) Li, Y.; Di, J.; Ma, C.; Zhang, J.; Zhong, J.; Wang, K.; Xi, T.; Zhao, J. Quantitative Phase Microscopy for Cellular Dynamics Based on Transport of Intensity Equation. *Opt. Express* **2018**, *26* (1), 586.

(39) Goodman, J. W. *Introduction to Fourier Optics*, 3rd ed.; Roberts & Company Publishers: Englewood, CO, 2005.

(40) Chang, B.; Leussink, P.; Jensen, F.; Hübner, J.; Jansen, H. DREM: Infinite Etch Selectivity and Optimized Scallop Size Distribution with Conventional Photoresists in an Adapted Multiplexed Bosch DRIE Process. *Microelectron. Eng.* **2018**, *191*, 77−83.

(41) Vo, S.; Fattal, D.; Sorin, W. V.; Peng, Z.; Tran, T.; Fiorentino, M.; Beausoleil, R. G. Sub-Wavelength Grating Lenses with a Twist. *IEEE Photonics Technol. Lett.* **2014**, *26* (13), 1375−1378.

(42) Li, S.-Q.; Xu, X.; Maruthiyodan Veetil, R.; Valuckas, V.; Paniagua-Dominguez, R.; Kuznetsov, A. I. Phase-Only Transmissive Spatial Light Modulator Based on Tunable Dielectric Metasurface. *Science (Washington, DC, U. S.)* **2019**, *364* (6445), 1087−1090.

(43) Shirmanesh, G. K.; Sokhoyan, R.; Wu, P. C.; Atwater, H. A. Electro-Optically Tunable Multifunctional Metasurfaces. *ACS Nano* **2020**, *14* (6), 6912−6920.

(44) Zou, C.; Staude, I.; Neshev, D. N. Tunable Metasurfaces and Metadevices. *Dielectr. Metamaterials* **2020**, 195−222.